



Bifurcation aspect of polygonal coherence over transitional Reynolds numbers in wide-gap spherical Couette flow

Fumitoshi Goto,¹ Tomoaki Itano ,^{2,*} Masako Sugihara-Seki ,^{2,3} and Takahiro Adachi ⁴

¹Graduate School of Science and Engineering, Kansai University, Osaka 564-8680, Japan

²Department of Pure and Applied Physics, Faculty of Engineering Science, Kansai University, Osaka, 564-8680, Japan

³Graduate School of Engineering Science, Osaka University, Osaka 560-8531, Japan

⁴Department of Systems Design Engineering, Akita University, Akita, 010-8502, Japan



(Received 17 August 2021; accepted 5 November 2021; published 22 November 2021)

This study numerically investigates the bifurcation aspect of the wide-gap spherical Couette flow (SCF), with an emphasis on the competition among polygonal coherence with different wave numbers observed over transitional Reynolds numbers. Focusing on a representative case, the half-radius ratio $\eta = 1/2$, we confirm that the axisymmetric state becomes unstable over the first transitional Reynolds number at which the fourfold spiral state bifurcates, using the continuation method based on the Newton–Raphson algorithm. The Galerkin–spectral method was employed to numerically solve the governing equations. It is found that the threefold spiral state bifurcates from the axisymmetric state at a slightly higher Reynolds number than the first transitional Reynolds number. The attraction of the threefold spiral state expands rapidly with an increase in the Reynolds number, which is determined by verifying the distance of the unstable periodiclike state to both spiral states in the state space. This aspect of the state space explains the experimentally bistable realization of different equilibrium states over the first transitional Reynolds number. This study also found that the periodiclike state is composed of the three- and fourfold spiral states, similar to a beat with two different frequencies.

DOI: [10.1103/PhysRevFluids.6.113903](https://doi.org/10.1103/PhysRevFluids.6.113903)

I. INTRODUCTION

An incompressible Newtonian fluid confined between concentric spherical boundaries rotating differentially, namely, the *spherical Couette flow* (SCF), is one of the canonical flows. The SCF is a configuration applicable to astrophysical and geophysical flows in the planetary core, atmosphere, and ocean. Stimulated by geophysical issues, experimental studies on the SCF were initiated by a few pioneers during the last quarter of the past century [1–7]. In particular, the case involving a rotating inner sphere and stationary outer sphere has been largely investigated; this case is controlled by the Reynolds number conventionally defined as $\text{Re} = r_{\text{in}}^2 \Omega_{\text{in}} / \nu$. Based on early investigations with several different combinations of spherical boundaries and various radii, it has been pointed out that SCF is fairly complicated compared to the cylindrical Taylor–Couette flow, despite the apparent similarity [8,9]. This difference is likely attributed to the presence of the meridional circulation and inflection point in the azimuthal profile in the hemisphere, which become more influential in the case of the larger gap between boundaries, that is, a small radius ratio. The case of a small radius ratio $\eta \leq 3/4$, which has been conventionally named “*wide-gap*” or “*thick layer*,” exhibits somewhat puzzling sequential transitions to turbulence involving nonuniqueness and hysteresis.

*itano@kansai-u.ac.jp

The first transition in a wide-gap SCF is triggered by the polygonal traveling waves, which are similar to the flow between two rotating planar disks. In general, a rotating shear flow always favors polygonal coherence around the poles. Regular polygonal patterns in the polar jet streams on Jupiter and Saturn were observed by recent spacecraft missions, which are relevant to the polygonal coherence in an SCF [10]. The observed polygonal waves in a wide-gap SCF, which form a sinusoidal disturbance at the midlatitudes propagating at a significantly low angular phase velocity in the azimuthal direction, were visualized as a spiral pattern with m equally spaced arms extending from the poles to the equatorial zone in each hemisphere. The transitional Reynolds numbers reported in a previous experimental study were $\text{Re}_{\text{cr}} = 2628$ ($m = 6$) at $\eta = 3/4$, $\text{Re}_{\text{cr}} = 1244$ ($m = 5$) at $\eta = 2/3$, and $\text{Re}_{\text{cr}} = 489$ ($m = 4$) at $\eta = 1/2$, where m was the azimuthal wave number at the critical Reynolds number [11]. It was confirmed that some of these values align remarkably well with theoretical predictions based on linear stability analysis [12–14]. A recent investigation with a further increase in the Reynolds number suggested relaminarization, nonuniqueness, and hysteresis in successive transition processes in an SCF [15–18]. These aspects in a wide-gap SCF can be regarded as a type of competition among different polygonal structures, which plays an important role in the route to turbulence. For example, Wulf *et al.* investigated successive transition processes undergoing several mode changes and concluded that the Ruelle-Takens-Newhouse scenario, associated with a few polygonal modes, represented a route to turbulence in a wide-gap SCF [16]. The variety of routes to turbulence still remains an open question in SCF.

Here, we focus on a representative but insufficiently investigated radius ratio, $\eta = r_{\text{in}}/r_{\text{out}} = 1/2$. Belyaef *et al.* estimated the first transitional Reynolds number $\text{Re}_{\text{cr}} = 460$ at $\eta = 1/2$ based on experimental studies of the power spectra of an SCF using laser Doppler velocimetry [9]. The emerged flow consisted of four vortices ($m_{\text{cr}} = 4$) in every hemisphere, displaced in staggered rows with respect to the equator. By quasistatically increasing Re further, a new wave regime emerged at the second transitional Reynolds number characterized by the $m = 3$ regime instead of the $m = 4$ regime, via a period doubling bifurcation of $m = 4$ with a subharmonic frequency. However, the $m = 3$ regime attained at a higher Reynolds number can be quasistatically maintained near the first transitional Reynolds number with reorganization of the $m = 4$ regime. This hysteresis was observed in the relatively low Reynolds number range, as previously reported by Belyaef and Yavorskaya [19]. They also suggested that a decrease in Re after an abrupt change in Re from $\text{Re} < 550$ to $\text{Re} > 660$ creates a temporal chaotic regime. The further decrease in Re from the chaotic state leads to an irreversible transition for a spatial structure with $m = 3$ (see Fig. 1 in Ref. [19]). In an overview of experimental and numerical studies, including the case of $\eta = 1/2$, Junk and Egbers concluded that the transitional Reynolds number was 489 and pointed out that similar flow regimes with a small number of spiral waves were observed before the flow became turbulent at a higher Reynolds number [11].

The primary motivation of the current work is to study the exchange of the stability of the $m = 3$ and $m = 4$ regimes at a representative radius ratio $\eta = 1/2$, which has been solved insufficiently. The aforementioned experimental observation implies that the $m = 4$ regime originates in the axisymmetric state and becomes stable over the first transitional Reynolds number, where the axisymmetric state is unstable. However, it is plausible that the $m = 3$ regime does not originate in the $m = 4$ regime and instead bifurcates from the unstable axisymmetric state. From the viewpoint of the deterministic dynamical system, it is significant how the $m = 3$ regime is established as a stable state over the second critical Reynolds number. Through the present study, we will elucidate the formation of the $m = 3$ regime in the state space, which has remained unclear thus far.

The remainder of this paper is organized as follows. In the next section, we briefly describe the nondimensionalized governing equations and numerical setup of our system. In Sec. 3, we present the numerically obtained nonaxisymmetric states and discuss the morphology of the vortex in comparison with previous studies. In the latter part of the section, the $m = 4$ and $m = 3$ states are exactly explored using the Newton–Raphson algorithm, and the first and second transitional Reynolds numbers are specified. We numerically confirm the bistability of these regimes and discuss

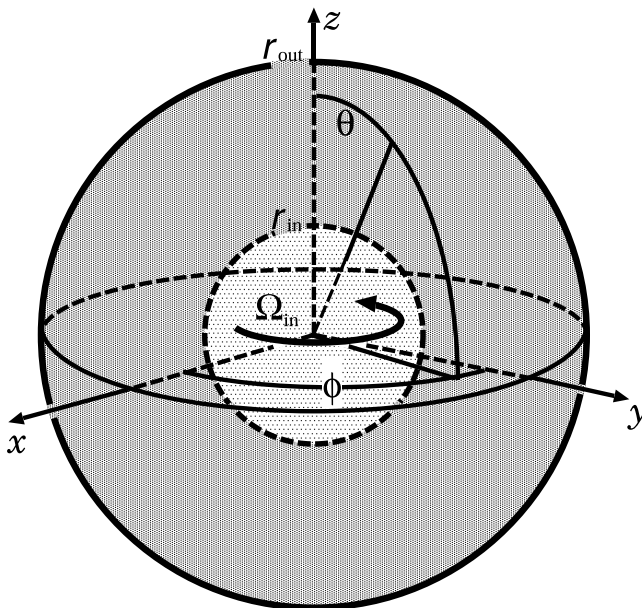


FIG. 1. Configuration of the present study.

the basin of attraction of nonaxisymmetric states. The paper concludes with brief remarks on the unstable saddlelike state between these states.

II. FORMULATION

The spherical coordinate represented by the radial, zenith, and azimuthal components, (r, ϑ, φ) , is centered at the origin. The incompressible fluid is confined between the inner and outer spheres with radii r_{in} and r_{out} , respectively, as shown in Fig. 1. The inner sphere rotates at a constant angular velocity Ω_{in} with respect to the z axis. The nondimensional geometrical parameter is either the gap ratio $\beta = (r_{\text{out}} - r_{\text{in}})/r_{\text{in}}$ or aspect ratio $\eta = r_{\text{in}}/r_{\text{out}}$.

The Galerkin-spectral method was employed to numerically solve the governing equations,

$$\frac{\partial \mathbf{u}}{\partial t} + (\mathbf{u} \cdot \nabla) \mathbf{u} = -\frac{1}{\rho_0} \nabla p + \nu_0 \nabla^2 \mathbf{u},$$

under the incompressible condition $\nabla \cdot \mathbf{u} = 0$. Due to the divergence-free constraint, toroidal and poloidal decomposition were invoked with regard to the radial direction, $\mathbf{u}(\mathbf{r}) = u_0(r, \theta) \mathbf{e}_\phi(r, \theta) + \nabla \times \{-r\boldsymbol{\Psi}(\mathbf{r}) + \nabla \times [r\boldsymbol{\Phi}(\mathbf{r})]\}$, where the magnitude of the Stokesian shear flow $u_0(r, \theta)$ is proportional to Ω_{in} and satisfies $\nabla^2(u_0 \mathbf{e}_\phi) = 0$, boundary conditions, $u_0(r_{\text{in}}) = r_{\text{in}} \Omega_{\text{in}}$, and $u_0(r_{\text{out}}) = 0$ [20]. Hereafter, the governing equation is nondimensionalized by the gap half-width $\Delta r = (r_{\text{out}} - r_{\text{in}})/2$ and the viscous diffusion time $\Delta r^2/\nu_0$. Therefore, the system is uniquely determined only by the geometrical parameter $\eta = r_{\text{in}}/r_{\text{out}}$ and Reynolds number Re . The toroidal and poloidal components are spatially expanded into a series of spherical harmonics $Y_l^m(\theta, \phi)$ with a polar wave number l and azimuthal wave number m through the aid of numerical libraries on spherical harmonics utilizing the Gauss-Lobatto collocation method [21,22]. Adapting the second-order Adams–Bashforth method, complemented by Crank–Nikolson for temporal discretization, we converted the nondimensionalized governing equation to an equivalent inhomogeneous Helmholtz equation. This Helmholtz equation is equivalent to a set of linear algebraic equations for the expansion coefficients $\Psi_{l,m,n}$ and $\Phi_{l,m,n}$ with the expansion into a series of modified

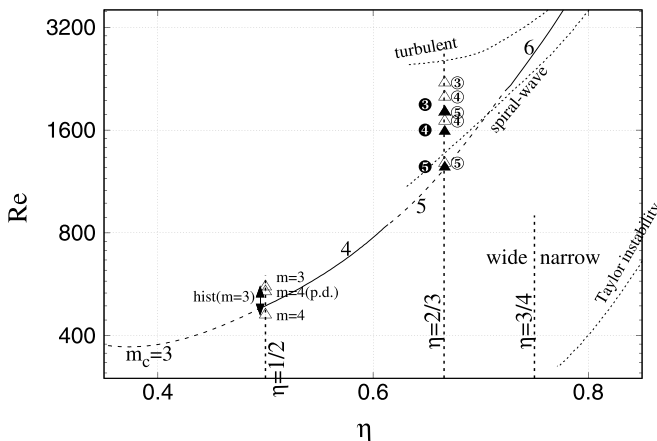


FIG. 2. SCF experiences the first transition on the route to turbulence in two different manners depending on the value of the geometrical parameter, η . The solid and dashed curves are the neutral curve of the axisymmetric state against an infinitesimal perturbation of the indexed even and odd azimuthal wave numbers, respectively. The numbers in the circles and triangles indicate the wave numbers of the spiral state observed in previous studies.

Chebyshev polynomials $(1 - y^2)^k T_n(y)$ ($k = 1$ for Ψ and $k = 2$ for Φ), where $y = (r - r_0)/\Delta r$ and $r_0 = \frac{r_{\text{in}} + r_{\text{out}}}{2}$. This was also used in our previous study [23]. This set of equations can be solved numerically using the LAPACK libraries [24]. Unless noted, we used the truncation levels $(l_{\text{max}}, m_{\text{max}}, n_{\text{max}}) = (30, 30, 32)$.

The developed numerical code [25] was validated for $\text{Re} < 600$ using a quantitative comparison with previous experimental and numerical results [14,16,17]. Numerical integration was used to obtain some equilibrium states at $\eta = 1/2$ around the transitional Reynolds numbers, beginning initially with a Stokesian flow with a small disturbance that was artificially generated by a series of random numbers. The basic laminar flow preferred under the first transitional Re consisted of the Stokesian shear flow perturbed by two azimuthal momentum cells in the northern and southern hemispheres. These were divided by a strong and local radial outward flow developing at the equatorial zone via the inertial (centrifugal) force of the rotating inner sphere. The basic laminar flow satisfied the axisymmetry $\frac{\partial}{\partial \phi} \Phi = \frac{\partial}{\partial \phi} \Psi = 0$ and equatorial symmetry $[\Phi(\pi - \theta), \Psi(\pi - \theta)] = [\Phi(\theta), -\Psi(\theta)]$. A fluid element initially confined in a hemisphere travels from the equator to the pole along the outer spherical boundary and then back to the equator along the rotating inner boundary. It was quantitatively confirmed that the magnitudes of the u_r and u_ϕ components of the numerically obtained axisymmetric flow aligned with those in a previous numerical study, with an error of a few percentage points [14]. As Hollerbach *et al.* reported, the magnitude of the radial component obtained numerically is comparable to that of the azimuthal component near the equator, which is characteristic of a wide-gap SCF but not narrow-gap cases [14].

III. RESULTS

With an increase in the Reynolds number, the SCF experiences the first transition on the route to turbulence in two different manners depending on the value of the geometrical parameter, as shown in Fig. 2. In the narrow-gap cases ($\eta > 3/4$), the transition is primarily initiated by axisymmetric Taylor vortices with successive instability, as observed in the cylindrical Taylor–Couette flow. Conversely, in the wide-gap cases ($\eta < 3/4$), the first transition is triggered by nonaxisymmetric secondary waves extending from the poles. The solid and dashed curves, which were reconstructed

based on values read from the graph in Ref. [14], are the neutral curves of the axisymmetric state against an infinitesimal perturbation of the indexed even and odd azimuthal wave numbers, respectively. The number of waves in a hemisphere at the transition is determined by the value of η and can be calculated by the linear stability analysis of the axisymmetric state. The numbers in the circles and triangles indicate the wave numbers of the spiral state observed in previous studies (Ref. [9] at $\eta = 1/2$ and Refs. [15,18] at $\eta = 2/3$), and they are located at the values (η, Ra) where the state was obtained experimentally or numerically.

Egbers and Rath employed experimental studies for several values of η in “*narrow-gap*” cases and found that the transition was initiated by the axisymmetric Taylor vortices with successive instability where $\eta > 3/4$, as observed in the cylindrical Taylor–Couette flow [15]. However, in “*wide-gap*” cases, the first transition was triggered in the absence of Taylor vortices by the nonaxisymmetric secondary waves extending from the poles where $\eta < 3/4$. The flow structure of the secondary wave consisted of a set of sinusoidal waves at the equator traveling in the azimuthal direction, which connected with the spiral disturbance extending in each hemisphere from the poles. Hereafter, we refer to the secondary wave with wave number m , which is the number of spiral waves extending from a pole, as an *m-fold spiral state*. The dependencies of the transitional Reynolds number on the value of η are listed in Ref. [11]. The wave number m selected at the first transition depends on the value of η . In the wide-gap case, the larger the value of η , the larger is the wave number.

Moreover, an experimental study conducted considering $\eta = 2/3$ reported that a further increase in the Reynolds number caused a successive sequence of transitions with a decrease in the wave number [15]. In other words, a spiral state with a smaller wave number was dominant as the Reynolds number increased. They reported that $m = 5$, $m = 4$, and $m = 3$ were observed at $Re = 1250$, $Re = 1600$, and $Re = 1900$, respectively. Clearly, the system exhibited a somewhat complicated hysteresis at these successive transitional Reynolds numbers. This hysteresis has also been reported in a numerical study considering $\eta = 2/3$, where $m = 5$ was obtained at $Re = 1280$, $m = 4$ at $Re = 1700$, $m = 5$ at $Re = 1800$, $m = 4$ at $Re = 2000$, and $m = 3$ at $Re = 2200$ [18]. This is represented by the numbers marked with circles at $\eta = 2/3$ in Fig. 2. The critical wave number at the first transitional Reynolds number was determined by η , whereas the ratio of the representative magnitude of the meridional circulation to the rotational speed of the inner sphere affected a successive sequence of transitions [25]. The increase in Re primarily enhanced the meridional circulation, whereas mixing in the gap induced a nonaxisymmetric flow, weakening the circulation. Once Re exceeds a critical value, a further increase in Re enhancing the mixing reduces the meridional circulation, which may lead to a spiral state with a reduced wave number. The decrease in the wave number of the nonaxisymmetric flow may be attributed to the reduction in the ratio of the meridional circulation to the inner sphere rotational speed.

Previous experimental and numerical studies have shown that hysteresis over the transitional Reynolds number is common in wide-gap SCFs. This implies that our system with $\eta = 1/2$ is a bistable system, where different stable spiral states are attained from different initial states. Based on an experimental study of the appearance of a single frequency in the power spectra, Belyaef *et al.* estimated the first transitional Reynolds number at $\eta = 1/2$ to be 460 with $m = 4$ [9]. They reported that an equilibrium state characterized by $m = 3$ vortices was realized over $Re = 556$ instead of $m = 4$ vortices, via a period doubling bifurcation excited by a subharmonic frequency over $Re = 538$. Moreover, they studied the lower Re limit that the $m = 3$ vortex regime survives by decreasing Re from $Re = 556$. This regime was not realized until the $m = 4$ vortex regime reappeared at $Re = 462$. This suggests that our system with $\eta = 1/2$ is also a bistable system over a certain second transitional Reynolds number. The first transitional Reynolds number at $\eta = 1/2$ was solved as $Re = 489$ in later studies [11,12]. Additionally, it should be noted that the wave number selected at the first transition in the case of $\eta = 1/2$ is $m = 4$, whereas the first transition at $\eta \lesssim 0.5$ is triggered by the $m = 3$ vortex regime [14]. This may be relevant to the competition between the $m = 3, 4$ vortex regimes near the first transition at $\eta = 1/2$.

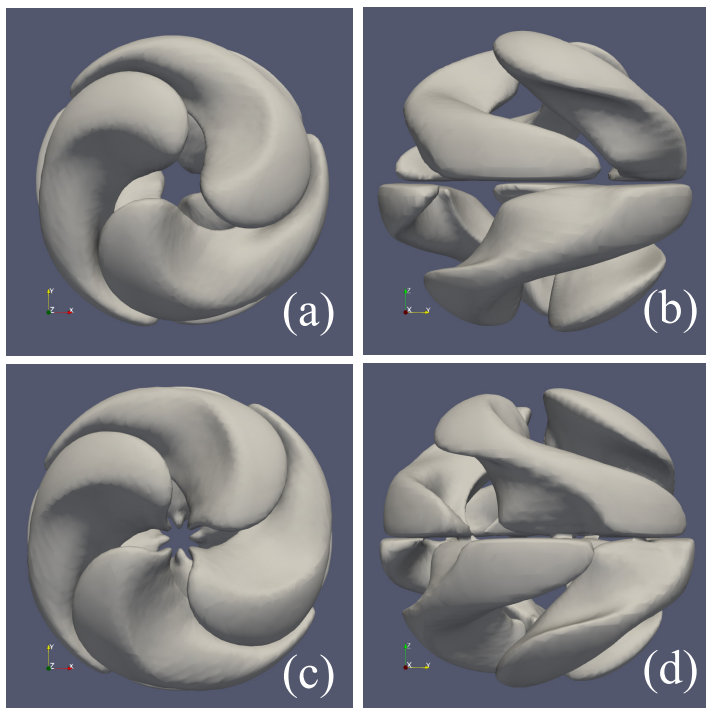


FIG. 3. Views of (a) polar threefold, (b) equatorial threefold, (c) polar fourfold, and (d) equatorial fourfold.

First, we carried out numerical trial computations at $\eta = 1/2$ by initially reducing all modes in the expansion coefficients of Φ and Ψ , except for $m = 0, 3, 4$. The computations at $\text{Re} = 560$ approximately settled in either the threefold and fourfold spiral states, depending on the disturbance in the initial condition. This implies that the three- and fourfold spiral states are stable attractors and that the basic state is a repeller. The obtained m -fold spiral states spontaneously satisfy $\Phi(r, \theta, \phi + 2\pi/m) = \Phi(r, \theta, \phi)$ and $\Psi(r, \theta, \phi + 2\pi/m) = \Psi(r, \theta, \phi)$. In addition, the flow pattern appearing in both hemispheres shifted toward each other by half the wavelength, such that the reflection symmetry to the equatorial plane, $\Phi(r, \pi - \theta, \phi) = -\Phi(r, \theta, \phi)$ and $\Psi(r, \pi - \theta, \phi) = \Psi(r, \theta, \phi)$ were satisfied. Taking into account these symmetries and the assumption of a rotating wave solution with a constant angular velocity, ω_ϕ , we substituted $\frac{\partial}{\partial t} = -\omega_\phi \frac{\partial}{\partial \phi}$ in the original governing equation, where the solution was assumed to constantly rotate around the z axis along the positive ϕ direction. A Galerkin-type reduced quadratic equation was deduced from the substitution for the expansion coefficients $\Psi_{l,m,n}$ and $\Phi_{l,m,n}$. Here, the freedom of ω_ϕ for the m -fold spiral state could be specified by fixing the azimuthal phase of the state. We subsequently solved the quadratic equations using the iterative Newton–Raphson method with the aid of LAPACK libraries [24]. The polar and equatorial views of the three- and fourfold spiral states were converged at $(\eta, \text{Re}) = (1/2, 490)$ and are visualized in Fig. 3 by an isosurface of the Φ deviation from the mean value. These states satisfy not only the m -fold symmetry with respect to a pole but also a reflection symmetry with respect to the equatorial plane. Note that the time constant of the least stable mode of the spiral states tends to almost vanish, particularly near the transitional Reynolds numbers. The Newton–Raphson algorithm has an advantage over the direct numerical simulation in that it is able to solve a less stable state. This enabled us to solve the phase angular velocity and obtain the states with a small time constant, which could be principally traceable using a long-term simulation.

We continuously obtained the threefold and fourfold spiral states using the Newton-Raphson algorithm by gradually varying Re from the transitional Reynolds number up to $\text{Re} = 800$. For each

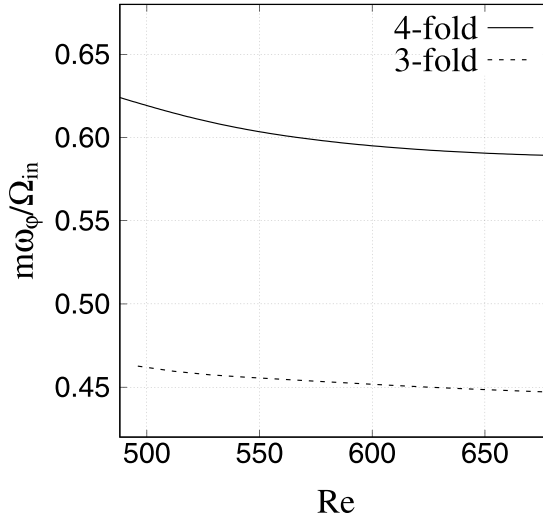


FIG. 4. The dimensionless frequencies against Re , calculated from the phase angular velocities of $m = 3$ -fold and $m = 4$ -fold spiral states for $\eta = 1/2$, decreased with an increase in Re .

Re , the phase angular velocity ω_ϕ converged to a value through stepwise iterations of the method. The dimensionless frequency, $m\omega_\phi/\Omega_{in}$, is defined from the ratio of the phase angular velocity ω_ϕ of the obtained state to the inner sphere angular velocity Ω_{in} ; this was plotted against the Reynolds number, as shown in Fig. 4. The frequencies for the four- and threefold states at $Re = 490$ and $Re = 496$ are 0.623 and 0.463, respectively. They gradually decrease with the increase in Re . Note that these coherent patterns rotate in the azimuthal direction with almost identical and relatively low angular velocities, approximately one sixth of the inner sphere rotation. The experimentally obtained value of the dimensionless frequency would appear as sharp peaks in the power spectra if a pointwise velocity signal of the flow was measured experimentally by using laser Doppler velocimetry to monitor the transition to chaos by detecting the broadening of these spectral lines. In particular, the frequency for the fourfold spiral state near the first transition was measured as 0.614 in a previous experiment, which is in reasonable agreement with the present numerical result [19]. As shown in Fig. 4, the dimensionless frequency gradually decreases as the Reynolds number increases, which also resembles the behavior in Fig. 1, as reported by Belyaef and Yavorskaya [19].

The transitional Reynolds number for $\eta = 1/2$ was first specified as $Re_{cr} = 460$ by Belyaef *et al.* [9]. This was later numerically refined by Dumas [12] and Hollerbach [14], and experimentally refined by Markus and Egbers [11] to be $Re_{cr} = 489$. The norm of the nonaxisymmetric components of Φ for the threefold and fourfold spiral states is defined as the integral of the squared velocity over the whole volume $\int |\Phi_{\text{antimirror},3D}|^2 dv$, where $\Phi_{\text{antimirror},3D} = \frac{1}{2} \sum_{m \neq 0} [\Phi_m(r, \theta, \phi) - \Phi_m(r, \pi - \theta, \phi)]$, as shown in Fig. 5. In the present calculation, the three- and fourfold spiral states converge to the axisymmetric states at $Re_4 = 486$ and $Re_3 = 487$, respectively. The three- and fourfold spiral states bifurcate from the axisymmetric state at different transitional Reynolds numbers, i.e., $Re = Re_3$ and $Re = Re_4$, respectively, where $Re_4 < Re_3$.

The arithmetic discrepancy in the critical Reynolds number between the previous and present studies is attributed to the difference in the numerical truncation. We confirmed that as the truncation level for the spherical polynomials increased from 30 to 60, the fourfold and threefold spiral states converged to the axisymmetric states at $Re_4 = 489$ and $Re_3 = 491$, respectively. Table I shows the convergence of the critical Reynolds number against the truncation and the ratio of the torque acting on the inner sphere to that of the Stokesian flow at $Re = 560$.

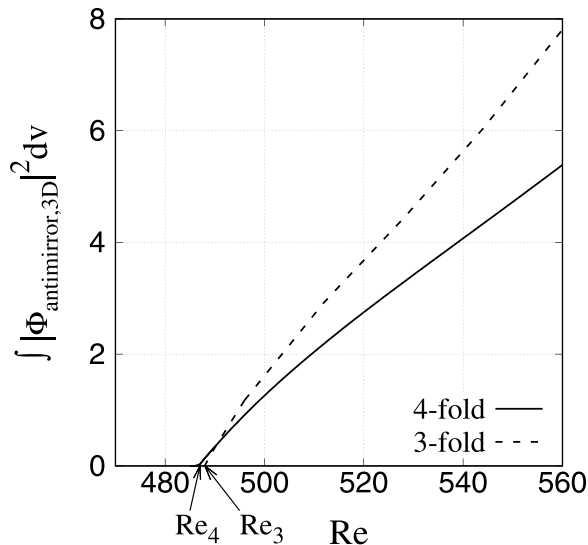


FIG. 5. Norm of the antimirror component of Φ with $m \neq 0$ plotted against Re for the three- and fourfold spiral states obtained at $\eta = 1/2$.

IV. DISCUSSION

The degree of m -fold spiral states can be measured by the magnitude of $X_m^2 = \int dv |\Phi_m|^2$ and $\Phi_m(r, \theta, \phi) = \sum_l \Phi_{l,m}(r) Y_l^m(\theta, \phi)$. Let us project the full state space of our system into a reduced space spanned by X_3 and X_4 . Note that the time evolution of the state is illustrated as a trajectory in the projection and that the three- and fourfold spiral states correspond to fixed points on the abscissa and ordinate, respectively. The basic state located at the origin of the map constitutes an unstable equilibrium over the first transitional Reynolds number. We numerically confirmed in advance that the three- and fourfold states were stable and that the basic laminar state was unstable for Reynolds numbers in the present study. Thus, both states were not only equilibrium states but also attractors in the state space, such that any infinitesimal perturbation against either equilibrium state decreased asymptotically. Consequently, there must be at least one subspace (a super surface in the full state space) that separates the basins of these attractors. We will hereafter refer to this as a *basin boundary* between the three- and fourfold spiral states.

Here, we will obtain the basin boundary in the map by employing an edge-tracking or shooting method, which was originally established as a tool to find an unstable steady solution embedded in

TABLE I. The convergence of the spiral state against the truncation level of spherical harmonics. (upper) The critical Reynolds number of three- and fourfold spiral states. (lower) The convergence of the nondimensionalized torque of three- and fourfold spiral states at $Re = 560$ against the truncation level of spherical harmonics, where the nondimensionalized torque is defined as the ratio of the torque acting on the inner sphere to that of the Stokesian flow analytically expressed.

L_{\max}	30	45	60
threefold	487.9	491.3	491.4
fourfold	486.7	488.8	488.8
threefold	3.126	3.133	3.134
fourfold	3.128	3.138	3.139

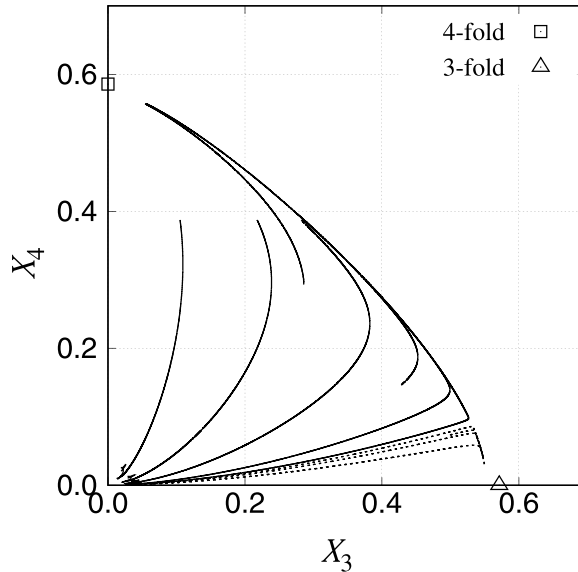


FIG. 6. Time variation of the system at $\text{Re} = 490$ projected in the reduced space spanned by X_3 and X_4 . The square on the ordinate indicates the fourfold spiral state bifurcated at $\text{Re} = \text{Re}_4$ from the axisymmetric state on the origin. The triangle on the abscissa indicates the threefold spiral state performed at $\text{Re} = \text{Re}_3$. The trajectories indicated by the solid and dashed curves approach the four- and threefold spiral states, respectively.

a subcritical system, such as a planar Couette flow [26–29]. Hereafter, we denote the m -fold spiral states as \mathbf{x}_m . We used an intermediate state $\mathbf{x}_s = (1 - s)\mathbf{x}_3 + s\mathbf{x}_4$ as the initial condition for a trial run, where s was a parameter. In the full state space, the continuous set of the initial condition \mathbf{x}_s for $0 \leq s \leq 1$ corresponded to a line segment connecting the threefold and fourfold spiral states. The segment must intersect the basin boundary at least once because both equilibrium states at the ends of the line segment are stable. We adjusted the value of s such that the state approached neither the threefold nor fourfold spiral states for as long as possible. The edge-tracking indicated that the time evolution for $s < s_0$ asymptotically reached a threefold spiral state, while that for $s_0 < s$ reached a fourfold spiral state. It is significant that the asymptotic state starting from \mathbf{x}_s is only classified by the magnitude of s . An infinite period is needed for the crossing point $s = s_0$ for the trial run $\mathbf{x}(t)$ starting from \mathbf{x}_{s_0} to reach either attractor. Principally, the trajectory starting with $s = s_0$ stays on the basin boundary, which is also a high-dimensional space. Thus, the time variation of the state variables of the trajectory with s_0 could exhibit chaotic or turbulent behavior.

Trajectories on the projection obtained at $\text{Re} = 490$, which is close to the first transitional Reynolds number Re_4 at $\eta = 1/2$, are shown in Fig. 6. The time variation of the states starting at different initial conditions are indicated as curves, which separate either to the three- or fourfold spiral states at a saddle point on the heteroclinic orbit. Note again that the fourfold spiral state emerged at a smaller Reynolds number than the threefold spiral state. The basin boundary emerged as a hidden concave curve with a small slope, which is identified in the figure as a watershed among trajectories starting near the origin and finally approaching either one of the spiral states in the projection. It should also be noted that this basin boundary was closer to the abscissa than that obtained at $\text{Re} = 560$, as shown in Fig. 7. The threefold spiral state, which bifurcates at a slightly higher Reynolds number than the fourfold spiral state, has a relatively narrow basin of attraction compared to that of the fourfold spiral state at $\text{Re} = 490$. This hints that the threefold spiral state and an unstable equilibrium bifurcate simultaneously from the origin at $\text{Re} = \text{Re}_3$, where the threefold spiral state would be unstable otherwise. When the threefold spiral state bifurcates at $\text{Re} = \text{Re}_3$, a boundary is also formed between the basin of attraction of the three- and fourfold spiral states from

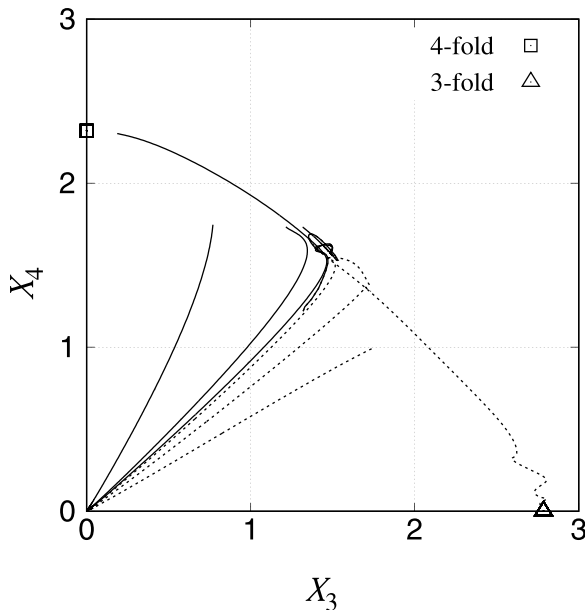


FIG. 7. Time variation of the system at $Re = 560$ projected in the reduced space spanned by X_3 and X_4 . Time variation of the states starting at different initial conditions are indicated as curves. The trajectories indicated by the solid and dashed curves approach the four- and threefold spiral states, respectively.

the unstable equilibrium. The trajectories concentrate on an arc connecting both the stable states before separating either to the three- or fourfold spiral states.

The trajectories on the projection obtained at $Re = 560$ are shown in Fig. 7. As the Reynolds number increased from the second transitional Reynolds number, the basin of the threefold spiral state expanded in the state space and then became comparable with that of the fourfold spiral state. From a deterministic viewpoint, the initial state, which is a point in the full state space, determined the final equilibrium that the state asymptotically reached. In most experiments, the initial condition is uncontrollable such that the initial point can be selected randomly in the state space. Therefore, the final equilibrium state may be estimated by the ratio of the volume of the basin boundary in the state space. The distance between the stable equilibrium state and unstable saddle point on the basin boundary in the full state space might be an index of the degree of attraction in the present bistable system. The reproducibility of the final asymptotic state can be constructed using the index.

The time variation of $X_4(t)$ for the trajectories obtained from the edge-tacking at $Re = 560$ are shown in Fig. 8. The unstable equilibrium state on the basin boundary was not a point but a periodiclike state composed of time-varying X_3 and X_4 components. The obtained value of s_0 was insignificant because it depended on both x_3 and x_4 , which were artificially adopted for the initial condition. However, the achieved equilibrium state, independent from the initial condition, is significant and characterizes the system at a given Re . Based on the visualization of this state, it was observed that the number of spiral arms extending from the poles to the equatorial zone in each hemisphere varied with time. If the two spiral states with slightly different angular phase velocities at $Re = 560$ would be superposed, the system would exhibit an interference in the time variation, observed as a beat between two distinct sounds with slightly different frequencies in terms of acoustics. The values of ω_ϕ/Ω_{in} were 0.1516 and 0.1503 for the three- and fourfold spiral states, respectively. Therefore, the period of the beat was $(2\pi/4/3)/\Delta\omega_\phi = 403$, which is comparable to the period observed in Fig. 8.

Based on the experimental observation of the sequential transitions obtained by the abrupt change in Re from $Re < 550$ to $Re > 660$, Belyaef and Yavorskaya [19] reported the existence of a regime

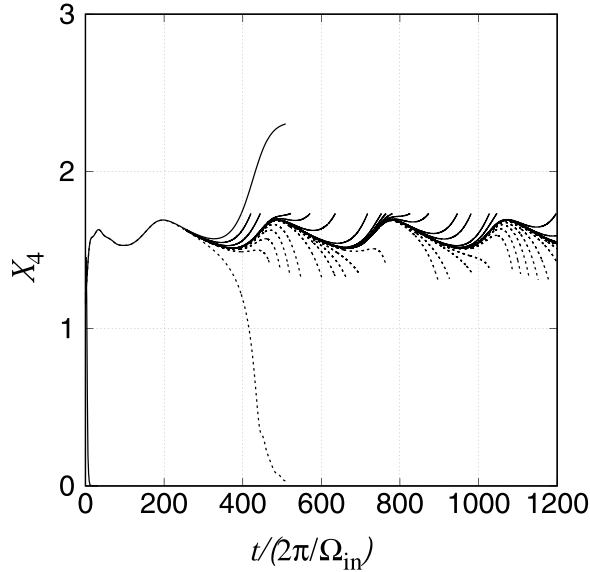


FIG. 8. Time variation of the degree of the fourfold spiral state, $X_4(t)$, obtained through the edge-tracking at $Re = 560$. Solid curves represent the trajectories starting from an intermediate state X_s for $s < s_0$ approaching a threefold spiral state. Dotted curves represent trajectories for $s > s_0$ for a fourfold spiral state.

with one half frequency of the fourfold state in the interval $710 < Re < 800$ and a periodic regime. This implies the possibility that the twofold spiral state may originate at a Reynolds number slightly larger than Re_3 . Considering this as an indication for obtaining the twofold state in the present study, we could obtain a twofold spiral state over $Re \sim 540$ using the Newton–Raphson algorithm by conducting several trial simulations under the restriction that the symmetries satisfied only by the twofold spiral state were imposed. There were at least two independent branches of the twofold spiral state over $Re \sim 590$. The difference in the angular phase velocities of these two independent branches was about one tenth of their absolute velocities, which could be recognized experimentally. Figure 9 shows the polar and equatorial views of the obtained twofold spiral state, which are visualized as an isosurface of the Φ deviation from the mean value. As is evident from the figure, the present twofold spiral state satisfies the aforementioned reflection symmetry to the equatorial plane; hence, a sinusoidal jet traveling in the azimuthal direction may be observed at the equator.

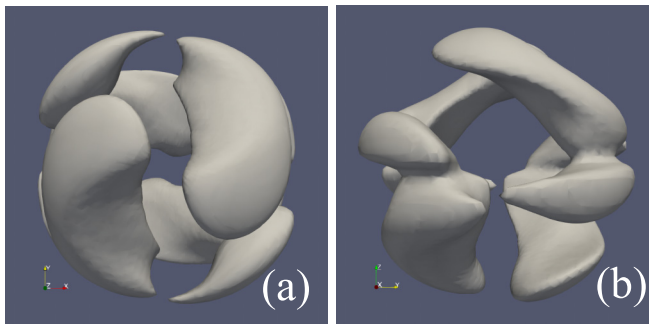


FIG. 9. Views of (a) polar and (b) equatorial twofold obtained at $Re = 576$.

This is remarkable, given that the axisymmetric state becomes unstable not only against the $m = 2$ sinusoidal disturbance in $1/4.8 \lesssim \eta \lesssim 1/3$ but also against the $m = 2$ varicose disturbance in $\eta \lesssim 1/4.8$, which was reported in Ref. [14]. It should be noted that a varicose disturbance is realized by another reflection symmetry to the equatorial plane, $[\Phi(r, \pi - \theta, \phi), \Psi(r, \pi - \theta, \phi)] = [\Phi(r, \theta, \phi), -\Psi(r, \theta, \phi)]$, where the flow pattern appearing in both hemispheres are distorted symmetrically by the wavelength. While the obtained twofold spiral state is probably rooted at the former sinusoidal disturbance, another twofold spiral state that is rooted at the latter might be obtained at larger Reynolds numbers at $\eta = 1/2$. In addition, it should be noted that the present twofold spiral state does not originate at the fourfold spiral state, because any state satisfying both the twofold and fourfold symmetries at the same time is axisymmetric. That is, the twofold and fourfold symmetries are mutually exclusive, so that it is impossible for either of the states to bifurcate from the other.

The trial simulation involving the start of these twofold spiral states yielded time-varying periodic states originating at the twofold spiral states. Relevant to the route to chaos in SCF, the multistability of the rotating waves with azimuthal wave number $m = 2, 3, 4$ and their successive transitions to the modulated periodic states have been recently investigated in the study on the continuation from wide-gap SCF to a magnetized spherical Couette system [30,31]. With regard to the unstable periodic states, these m -fold states are realized in sequential bifurcations, braking the azimuthal symmetry as the externally applied axial magnetic field strength varies. It should be noted that in the present study, without any external magnetic field, it is restricted by the symmetry that is satisfied only by the twofold spiral state in which these periodic states should principally be stable. The twofold spiral state may be stable or not in the full state space without the aforementioned restriction over $Re \sim 540$, where the three- and fourfold spiral states with their own basin of attraction are stable attractors. This subject remains for future study.

V. SUMMARY

The bifurcation aspect of a wide-gap SCF was numerically investigated, with an emphasis on the competition among polygonal coherence with various wave numbers observed over the transitional Reynolds numbers. We focused on a representative case, the half-radius ratio $\eta = 1/2$, by means of the continuation method based on the Newton–Raphson algorithm. This was used to confirm that the axisymmetric state became unstable over the first transitional Reynolds number Re_4 at which the fourfold spiral state bifurcated. It was found that the threefold spiral state successively bifurcated from the axisymmetric state at a slightly higher Reynolds number Re_3 than the first transitional Reynolds number.

The attraction of the threefold spiral state was guaranteed by a basin boundary consisting of a hidden unstable periodiclike state that bifurcates from the axisymmetric state at Re_3 , which forms a heteroclinic orbit connecting to the three- and fourfold spiral states in the state space. The attraction of the threefold spiral state expanded rapidly with an increase in the Reynolds number, which was verified using the distance from the unstable periodiclike state to both the spiral states in the state space. This aspect of the state space explains the experimentally bistable realization of different equilibrium states over the first transitional Reynolds number. It was also found that the periodiclike state was composed of the three- and fourfold spiral states, similar to a beat with two different frequencies. The validation of the present scenario under the other representative aspect ratio of the wide-gap SCF, such as $\eta = 2/3$ and $3/4$, is ongoing. Future studies should attempt to understand the roles that a combination of a few polygonal modes and periodic states plays along the route to turbulence in the wide-gap SCF under the Ruelle-Takens-Newhouse scenario.

ACKNOWLEDGMENTS

The authors thank Dr. Yamashita, Dr. Yokoyama, Prof. J. Seki, and Prof. N. Sugimoto for their valuable comments. We also thank Editage for English language editing. This work has been

supported in part by Grant-in-Aid for Scientific Research(C), JSPS KAKENHI Grant No. 20K04294. This work was also benefited from interactions within the RISE-2018 No.824022-ATM2BT of the European H2020-MSCA programme, which includes Kansai and Akita Universities.

-
- [1] S. Chandrasekhar, *Hydrodynamic and Hydromagnetic Stability* (Clarendon Press, Oxford, 1961).
 - [2] F. H. Busse, Patterns of convection in spherical shells, *J. Fluid Mech.* **72**, 67 (1975).
 - [3] A. Zebib, G. Schubert, J. L. Dein, and R. C. Pariwal, Character and stability of axisymmetric thermal convection in spheres and spherical shells, *Geophys. Astrophys. Fluid Dyn.* **23**, 1 (1983).
 - [4] S. Kida, K. Araki, and H. Kitauchi, Periodic reversals of magnetic field generated by thermal convection in a rotating spherical shell, *J. Phys. Soc. Jpn.* **66**, 2194 (1997).
 - [5] A. Sakuraba and M. Kono, Effect of the inner core on the numerical solution of the magnetohydrodynamic dynamo, *Phys. Earth Planet. Inter.* **1111**, 105 (1999).
 - [6] C. M. R. Fowler, *The Solid Earth* (Cambridge University Press, Cambridge, UK, 2004).
 - [7] F. Feudel, K. Bergemann, L. Tuckerman, C. Egbers, B. Fütterer, M. Gellert, and R. Hollerbach, Convection patterns in a spherical fluid shell, *Phys. Rev. E* **83**, 046304 (2011).
 - [8] B. R. Munson and M. Menguturk, Viscous incompressible flow between concentric rotating spheres, *J. Fluid Mech.* **69**, 705 (1975).
 - [9] Yu. N. Belyaev, A. A. Monakhov, S. A. Scherbakov, and I. M. Yavorskaya, Some routes to turbulence in spherical Couette flow, in *Proceedings of the Laminar-Turbulent Transition IUTAM-Symposium*, edited by V. V. Kozlov (Springer-Verlag, Berlin Heidelberg, New-York, Tokyo, 1984), pp. 669–676.
 - [10] D. A. Godfrey, A hexagonal feature around Saturn’s north pole, *Icarus* **76**, 335 (1988).
 - [11] M. Junk and C. Egbers, Isothermal spherical Couette flow, in *Physics of Rotating Fluids*, vol. 549 of *Lecture Notes in Physics*, edited by Christoph Egbers and Gerd Pfister (Springer, Berlin, 2000), pp. 215–233.
 - [12] D. Dumas and A. Leonard, A divergence-free spectral expansions method for three dimensional flows in spherical-gap geometries, *J. Comput. Phys.* **111**, 205 (1994).
 - [13] K. Araki, J. Mizushima, and S. Yanase, The nonaxisymmetric instability of the wide-gap spherical Couette flow, *Phys. Fluids* **9**, 1197 (1997).
 - [14] R. Hollerbach, M. Junk, and C. Egbers, Nonaxisymmetric instabilities in basic state spherical Couette flow, *Fluid Dyn. Res.* **38**, 257 (2006).
 - [15] C. Egbers and H. J. Rath, The existence of Taylor vortices and wide-gap instabilities in spherical Couette flow, *Acta Mech.* **111**, 125 (1995).
 - [16] P. Wulf, C. Egbers, and H. J. Rath, Routes to chaos in wide-gap spherical Couette flow, *Phys. Fluids* **11**, 1359 (1999).
 - [17] K. Nakabayashi, Y. Tsuchida, and Z. Zheng, Characteristics of disturbances in the laminar-turbulent transition of spherical Couette flow. I. Spiral Taylor-Görtler vortices and traveling waves for narrow gaps, *Phys. Fluids* **14**, 3963 (2002).
 - [18] S. Abbas, L. Yuan, and A. Shah, Simulation of spiral instabilities in wide-gap spherical Couette flow, *Fluid Dyn. Res.* **50**, 025507 (2018).
 - [19] Yu. N. Belyaev and I. M. Yavorskaya, Transition to stochasticity of viscous flow between rotating spheres, in *Nonlinear Dynamics and Turbulence*, edited by G. I. Barenblatt, G. Iooss, and D. D. Joseph (Pitman advanced publishing program, Boston, 1983); Spherical Couette flow: Transitions and onset of chaos, translated from *Izvestiya Akademii Nauk SSSR, Mekh. Zhidk. Gaza* 10 (1991).
 - [20] L. D. Landau and E. M. Lifshitz, *Fluid Mechanics: Vol. 6 (Course of Theoretical Physics) 2nd ed.* (Butterworth-Heinemann, Oxford, UK, 1987).
 - [21] N. Schaeffer, Efficient spherical harmonic transforms aimed at pseudospectral numerical simulations, *Geochem. Geophys. Geosyst.* **14**, 751 (2013).
 - [22] M. Frigo and S. G. Johnson, The design and implementation of FFTW3, *Proc. IEEE* **93**, 216 (2005).

- [23] T. Itano and S. C. Generalis, Hairpin Vortex Solution in Planar Couette Flow: A Tapestry of Knotted Vortices, [Phys. Rev. Lett.](#) **102**, 114501 (2009).
- [24] E. Anderson, Z. Bai, C. Bischof, S. Blackford, J. Demmel, J. Dongarra, J. Du Croz, A. Greenbaum, S. Hammarling, A. McKenney, and D. Sorensen, *LAPACK Users' Guide*, 3rd ed. (Society for Industrial and Applied Mathematics, Philadelphia, PA, 1999).
- [25] T. Inagaki, T. Itano, and M. Sugihara-Seki, Numerical study on the axisymmetric state in spherical Couette flow under unstable thermal stratification, [Acta Mech.](#) **230**, 3499 (2019).
- [26] T. Itano and S. Toh, The dynamics of bursting process in wall turbulence, [J. Phys. Soc. Jpn.](#) **70**, 703 (2001).
- [27] S. Toh and T. Itano, A periodic-like solution in channel flow, [J. Fluid Mech.](#) **481**, 67 (2003).
- [28] T. Schneider, J. Gibson, M. Lagha, F. D. Lillo, and B. Eckhard, Laminar-turbulent boundary in plane Couette flow, [Phys. Rev. E](#) **78**, 037301 (2008).
- [29] Y. Duguet, L. Brandt, and B. R. J. Larsson, Towards minimal perturbations in transitional plane Couette flow, [Phys. Rev. E](#) **82**, 026316 (2010).
- [30] F. Garcia and F. Stefani, Continuation and stability of rotating waves in the magnetized spherical Couette system: Secondary transitions and multistability, [Proc. R. Soc. A](#) **474**, 20180281 (2018).
- [31] F. Garcia, M. Seilmayer, A. Giesecke, and Frank Stefani, Four-Frequency Solution in a Magnetohydrodynamic Couette Flow as a Consequence of Azimuthal Symmetry Breaking, [Phys. Rev. Lett.](#) **125**, 264501 (2020).